07,13

Ti-Ni-Ta-based surface alloy synthesized on the TiNi-substrate through electron-beam method: structure and physical-mechanical properties

© F.A. D'yachenko, V.O. Semin, M.G. Ostapenko, L.L. Meisner

Institute of Strength Physics and Materials Science, Siberian Branch, Russian Academy of Sciences, Tomsk, Russia

E-mail: dfa@ispms.ru

Received February 22, 2023
Revised February 22, 2023
Accepted March 2, 2023

The structure and physical-mechanical properties of Ti-Ni-Ta-based surface alloy synthesized on the TiNi-substrate through additive thin-film electron-beam method have been studied. The synthesis of the surface alloy was carried out by 30-fold alternation of operations of deposition of a dopant film ($Ti_{60}Ta_{40}$ (at.%), ~ 50 nm thick) and liquid-phase mixing of the film/substrate using a pulsed low-energy high-current electron beam. It was found that Ti-Ni-Ta-based surface alloy, whose thickness is $\sim 1.8\,\mu$m, has an amorphous structure. It has been established that the surface alloy has ~ 2 and ~ 1.5 times higher values of microhardness H_{OP} and elastic modulus E_{OP} compared to the initial TiNi-substrate, but parameter of plasticity δ_h and shape recovery ratio η close to the substrate. It is shown that the nature of the change in physical-mechanical properties in Ti-Ni-Ta-based surface alloy and the transition zone depends on the number and thickness of the sublayers, as well as on the structural states of the phases in the sublayers. The evaluation of the mechanical compatibility of the surface alloy with the TiNi-substrate is given.

Keywords: Ti-Ni-Ta-based surface alloy, nickel titanium alloy, thin films, additive thin-film electron-beam synthesis, structure, physical-mechanical properties, strength and ductility parameters.

DOI: 10.21883/PSS.2023.04.56000.24

1. Introduction

Titanium nickelide-based alloys (TiNi alloys) are widely used to develop miniature products for healthcare and non-healthcare purposes (actuators, temperature sensors, implants, surgical armaments, etc. [1]). A downside of these alloys is degradation of their inelastic [2] and biochemical (corrosion resistance [3], biocompatibility [4]) properties in the process of multicycle operation. These properties depend on the condition of surface of the product and can be improved significantly by modifying its surface layer [4] or by synthesis of protective films or coatings on its surface [3].

The studies of [5–9] have demonstrated efficiency of the additive thin-film electron-beam method to synthesize multicomponent surface alloys (SA) to modify TiNi alloy surface for the purpose of improvement of its physico-mechanical and functional properties. The kernel of this method described in [5-9] consists in multiple alternation of deposition of a doping film with a pre-defined chemical composition of ($Ti_{70}Ta_{30}$ [5,6], $Ti_{85/70}Nb_{15/30}$ [7], $Ti_{60}Ta_{30}Si_{10}$ [8] and $Ti_{60}Nb_{30}Si_{10}$ [9] (at.%)) and with a certain thickness ($50-100$ nm) and liquid-phase mixing of film components and the substrate by pulse low-energy (≤ 30 keV) high-current (up to ~ 25 kA) electron-beam (LEHCEB) of microsecond duration ($\sim 2-4\,\mu$s). It has been shown that the synthesized multicomponent SAs based on Ti, Ni, Ta, Nb and Si have high potential for the use in the industry of miniature products for healthcare and non-healthcare purposes as protective barrier layers on the surface of TiNi alloys due to their biochemical (low concentration of nickel [5,7–9], high corrosion resistance [8,9]) and physico-mechanical (high strength and plasticity [6–9]) properties.

Concurrently with the tasks of studying functional properties, morphology of surface and structures of formed SAs not insignificant are the tasks related to the study of dependencies of changes in physico-mechanical properties. These tasks are non-trivial because the formed SAs are characterized by both single-layer structure [8,9] and multilayer structure [5–7,9] of consecutive sublayers with different thickness, phase composition and type of structure in the sublayers (nanocrystalline [5,6], amorphous [7–9], nanocomposite [7,9]).

An effective method to evaluate physico-mechanical properties (including inelastic properties) of surface layers with micron-order thickness is instrumented indentation. This method allows identifying differences in elastic and plastic deformation behavior in nanocomposite coatings [10], amorphous materials [11], as well as in multilayer composite systems of alternating amorphous and nanocrystalline layers [12], including materials with a gradient change in composition [10–12]. In the above-listed studies, thickness of systems under study was from $\sim 1-2\,\mu$m. The studies performed by now on bulk materials [13,14] and thin films [15,16] based on Ti-Ni that possess shape memory effect and superelasticity (SME-SE) have shown effectiveness of the use of this method for the evaluation of inelastic

deformation behavior of surface layers. Therefore, it seems effective to use the method of instrumented indentation for both the evaluation of physico-mechanical properties of SAs with a singlelayer/multilayer structure and the investigation of the effect of SA structure and properties on the inelastic properties of TiNi-substrate.

Some of the above-mentioned studies evaluated physico-mechanical properties using microhardness H_{OP} and modulus of elasticity E_{OP} measured with the indentation by sharp-tip Vickers pyramid indenters and Berkovich pyramid indenters following the Oliver–Pharr method [17]. The large differences in values of modulus of elasticity in austenite and martensite phases allow identifying these structural states in TiNi alloys [18]. In [14–16,19,20] it has been shown that an effective method of studying thin films, coatings or materials with gradient structures is the use of elastic-plastic parameters: the degree of shape recovery ratio η and plasticity parameter δ, which can be determined from $P-h$ experimental diagrams of „loading-unloading". In [14], with the use of η parameter, the interrelation has been noted for the first time between the recovery of indent and the SE effect, the possibility has been demonstrated to evaluate the SE using the η. In [15,16] it has been noted that this technique allows evaluating inelastic properties of thin films with SME-SE in [film/Si-substrate] systems where singlelayer and multilayer films of Ni-Ti [15,16], Ni-Ti-Cu and Ni-Ti-Cu/NiTi [15] have been produced by PVD methods. The parameter of plasticity δ determined by the Milman's method [19] characterizes the tendency of a material to deform irreversibly under exposure to loading by indenter. From the $P-h$ diagrams of „loading-unloading" in [20] the percentage of accumulated plastic deformation in the system of composite wear-resistant Cr/CrN/CrAlSiN-based coatings has been determined (thickness multilayer system was from ~ 4.12 to $\sim 4.55\,\mu$m).

In this study, to improve physico-mechanical and functional properties of miniature products made of TiNi alloys, a SA based on the Ti-Ni-Ta system using a doping film of $Ti_{60}Ta_{40}$ (at.%) is synthesized on the surface TiNi-substrate. Previously, in [5,6] the structure and physico-mechanical properties of a SA based on the same Ti-Ni-Ta system but using a doping film with other composition — $Ti_{70}Ta_{30}$ — have been studied. It has been shown in [6] that the synthesized SA, which has a multilayer structure of alternating sublayers of nanocrystalline and amorphous phases, has high physico-mechanical properties. It is found that the monotonous change in properties from high-strength layers of SA (microhardness of $H_{OP} \approx 8$ GPa, modulus of elasticity of $E_{OP} \approx 105$ GPa) to TiNi-substrate ($H_{OP} \approx 3.5$ GPa, $E_{OP} \approx 55$ GPa) is due to the formation of nanocomposite sublayers with close thicknesses (~ 300 nm). At the same time, in [21] it has been shown that an increase by ~ 10 at.% in the concentration of tantalum in the doping film results in amorphization of the synthesized SA structure throughout almost entire its thickness, which is important for solving application tasks.

Finally, when studying physico-mechanical properties of [SA/TiNi-substrate] systems, it is important to evaluate mechanical compatibility of the synthesized SA with the TiNi-substrate. Mechanical compatibility is a „general-purpose" term, which, by comparing properties (modulus of elasticity, plasticity, deformation reversibility) of the materials in question, is used to evaluate the closeness of characteristics of one material to another material. For example, in medical material science the mechanical compatibility is understood as closeness of elastic characteristics of the implant material to those of the bone tissue [22,23]. In this study, in the context of [SA/TiNi-substrate] system, the mechanical compatibility is understood as closeness of physico-mechanical properties of the SA and the TiNi-substrate. It is clear that when choosing methods of TiNi alloy surface modification, the methods should be used that provide formation of surface layers not only with improved characteristics but with high mechanical compatibility with the TiNi-substrate at the same time.

The purpose of this study is to find out the dependencies of change in physico-mechanical properties of the Ti-Ni-Ta system-based SA synthesized with the use of $Ti_{60}Ta_{40}$ (at.%) doping film on the surface of TiNi alloy by electron-beam method and to find out the interrelation between characteristics of the SA structure (phase composition, structural state, their changes along the depth) and its physico-mechanical properties. A special attention is paid to the SA compatibility with the TiNi-substrate.

2. Material, processing and research methods

In this study samples were used in the form of plane-parallel plates with sizes of $10 \times 10 \times 1$ mm made of TiNi alloy of TN-1 grade (MATEK-SPF, Russia), which were cut out by laser from the initial sheet semifinished product. Chemical composition of the alloy: $Ti-55.75\,Ni-0.035\,O-0.02\,C-0.003\,N-0.001\,H$ (wt.%); reverse martensite start temperature is $A_S = 308$ K. The surface of initial TiNi-substrate before the SA synthesis was chemically etched (in the solution of $HNO_3 + HF$ acids, 3 : 1 (vol.%)), electrolytic polished ($CH_3COOH + HClO_4$, 3 : 1 (vol.%)) and washed in an ultrasound bath (in distilled water for ~ 30 min.). To smooth the surface and to homogenize the surface layer, the pulsed LEHCEB-treatment was applied in the mode of surface melting (density of the electron beam energy was $E_s = 3.8$ J/cm^2, number of pulses was $n = 32$).

The surface Ti-Ni-Ta-alloy was formed on the TiNi-substrate (hereinafter sample with SA is refereed to as the sample with [TiNi-Ta_{40}]SA) in a single vacuum cycle in a „RITM-SP" modified automated facility (by „Mikrosplav" LLC, Russia) [24]. The $Ti_{60}Ta_{40}$ (at.%) film with a thickness of ~ 50 nm was deposited on the surface of TiNi-substrate by magnetron method simultaneously from two magnetrons by sputtering single-component targets of

pure Ti (99.95 wt.%) and Ta (99.95 wt.%) (Girmet, Russia). Composition of the deposited film was monitored by energy dispersive spectroscopy (EDS) (X-ACT silicon drift detector (Oxford Instruments, Great Britain)) using a LEO EVO 50 scanning electron microscope (SEM) (Zeiss, Germany) at an accelerating voltage of $U = 10$ kV. According to the measurements, the composition of film was consistent with the calculated composition ($Ti_{60}Ta_{40}$) with an accuracy of ± 2 at.%. The film was almost free from carbon, the oxygen concentration in it was not more than a few at.%. The liquid-phase mixing was performed using LEHCEB at $E_s = 2$ J/cm^2 and $n = 5$. The operations of film deposition and its pulsed electron-beam liquid-phase mixing with the TiNi-substrate were carried out in a single vacuum cycle. The number of synthesis cycles N were repeated 30 times without removing the TiNi-substrate from the working chamber of the plant. The temperature of the TiNi-substrate did not exceed 473 K by the end of the synthesis. Thus, the expected effective thickness of the synthesized [TiNi-Ta_{40}]SA was $\sim 1.5\,\mu$m.

Electron microscopy studies using bright and dark fields, microdiffraction analysis and nanodiffraction analysis were performed by a JEM-2100 transmission electron microscope (TEM) (JEOL, Japan) at an accelerating voltage of 200 kV. The size of the electron probe in microdiffraction and nanodiffraction modes was ~ 200 and ~ 12 nm, respectively. Foils for TEM studies were prepared in an EM 09100IS ion etching unit (JEOL, Japan) in the „cross-section" geometry. The composition of elements along the cross-section was determined by an accessory for EDS-microanalysis (X-Max SDD detector (Oxford Instruments, Great Britain)).

Strength and elastic-plastic parameters were determined by the method of instrumented indentation in a Nano Hardness Tester (CSM, Switzerland) equipped with a Vickers indenter (tetragonal diamond pyramid with an apex angle of $\alpha_V = 136°$). The test load profile is triangular. The duration of one „loading/unloading" cycle is $t = 60$ s, the indentation step is ~ 1 nm. The set of experimental data array for each load corresponded to three tests, followed by statistical averaging. The tests were carried out with two groups of samples (before and after surface modification), 6 samples in each group.

To study physico-mechanical properties of the [[TiNi-Ta_{40}]SA/TiNi-substrate] system, maximum loads $P_{\max}$ on the indenter were selected experimentally in the range from 5 to 300 mN (22 loads). Thus, with loadings in the range of 5–20 mN, with a maximum indentation depth $h_{\max}$ not more than ~ 500 nm, physico-mechanical properties of the [TiNi-Ta_{40}]SA were characterized. In the loading range of 25–200 mN properties of the [TiNi-Ta_{40}]SA were evaluated at a depth from ~ 500 nm to $\sim 1.8\,\mu$m, and properties of the transition zone between the SA and the TiNi-substrate a depth from ~ 1.8 to $\sim 2.5\,\mu$m were evaluated as well. In the loading range of 220–300 mN, physico-mechanical properties of the TiNi-substrate were evaluated in the adjacent area of the SA located at a depth of $\sim 2.5\,\mu$m from the surface.

Based on the $P-h$ diagrams of „loading/unloading" the strength and elastic-plastic parameters were determined depending on the maximum indentation depth $h_{\max}$. The microhardness H_{OP} and the modulus of elasticity E_{OP} were calculated by the method of Oliver-Pharr [17]. The plasticity parameter δ_h, which characterizes the tendency of a material to deform irreversibly under a load of P, was evaluated by the method of Yu.V. Milman described in [19]:

$$\delta_h = \frac{h_r}{h_{\max}} \times 100\%,$$

where h_r is depth of the formed indent after unloading; $h_{\max}$ is maximum indentation depth.

The η parameter characterizing the degree of shape recovery ratio was calculated by the method described in [14]:

$$\eta = \frac{h_{\max} - h_r}{h_{\max}} \times 100\%.$$

Average values of strength and elastic-plastic parameters for the initial TiNi-substrate at a depth greater than $\sim 2\,\mu$m are

$$H_{OP} = 3.5 \pm 0.5\,\text{GPa}, \quad E_{OP} = 55.0 \pm 2.5\,\text{GPa},$$

$$\delta_h = 55.0 \pm 5.0\% \quad \text{and} \quad \eta = 45.0 \pm 5.0\%.$$

The studies were carried out on the equipment of the „NANOTECH" Center of Equipment Sharing ISPMS SB RAS (Russia, Tomsk).

3. Results and discussion

3.1. Structure and composition of elements of the sample with [TiNi-Ta_{40}]SA

Fig. 1 and 2 show bright-field electron-microscopic images of the structures in the cross-section of the sample with [TiNi-Ta_{40}]SA. According to results of the studies, the synthesized layer is composed of the [TiNi-Ta_{40}]SA and the transition zone. At a depth of up to $\sim 1.8\,\mu$m from the surface the formed [TiNi-Ta_{40}]SA has a single-layer structure (outer layer I in Fig. 1). The transition zone is composed of three sublayers (II-III-IV) following one after another and differ by thickness, chemical and phase compositions, average grain size and grain orientation.

According to the microdiffraction pattern (Fig. 1, *c*), the [TiNi-Ta_{40}]SA is characterized by fully amorphous structure (Fig. 1, *a, b*) and contains defects: nanopores with sizes from ~ 7 to ~ 20 nm located at a depth of ≤ 500 nm from the surface at average distance of ~ 100 nm from each other (shown with arrows in Fig. 1, *a, b*). Results of the TEM/EDS-microanalysis along the cross-section of the sample with [TiNi-Ta_{40}]SA have shown (Fig. 3) that the composition of elements in layer I at a depth of ≤ 500 nm in average can be described by the following formula (at.%): $Ti_{\sim 49-48}Ni_{\sim 32-33}Ta_{\sim 19-18}$, and further it changes monotonously with decrease in the concentration of tantalum. Quantity of nickel on the surface is ~ 32 at.%,

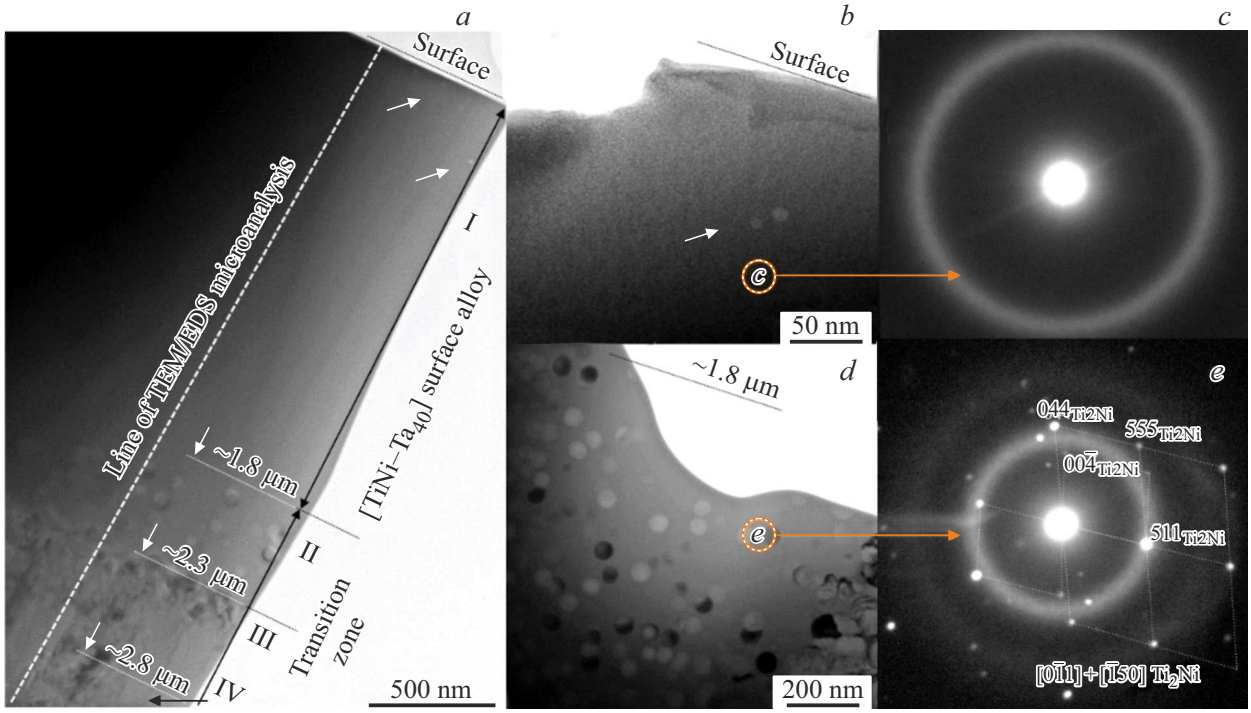

Figure 1. Bright-field images of structure of the sample with [TiNi-Ta_{40}]SA (a, b, d) and nanodiffraction pattern (c, e) from the [TiNi-Ta_{40}]SA (b) and the nanocomposite sublayer II (d).

which is ~ 1.5 times less than that in the initial TiNi-substrate. Previously, in [5,6] it has been shown that in TiNi-samples after formation of the surface Ti-Ni-Ta-alloy with the use of $Ti_{70}Ta_{30}$ (at.%) doping film the concentration of nickel in the surface layer with a thickness of ~ 400 nm from the surface turned to be less than expected and was ~ 10 at.%. It has been shown by the authors that such a significant nickel depletion in the near-surface areas is related to the multilayer nanocomposite structure of this SA.

Under amorphous layer I, at a depth from ~ 1.8 to $\sim 2.3\,\mu$m there is nanocomposite sublayer II with a thickness of not more than ~ 500 nm (Fig. 1, a, d). Inside sublayer II there are spherical nanocrystalline particle with sizes of ≤ 40 nm. The nanodiffraction analysis of individual particles has shown (Fig. 1, d, e) that nanocrystals, which are uniformly distributed within the amorphous matrix, belong to the Ti_2Ni phase (Pearson symbol cF96). Most of nanocrystals are located separately from each other and distributed in the amorphous matrix in a uniform manner. The concentration of tantalum in this sublayer decreases from ~ 10 to ~ 7 at.% (Fig. 3).

Sublayer III with a thickness of up to ~ 500 nm is located at a depth from ~ 2.3 to $\sim 2.8\,\mu$m and characterized by the eutectic type of structures. The concentration of tantalum in this sublayer decreases from ~ 7 to ~ 4 at.% (Fig. 3). As the interpretation of microdiffraction patterns has shown (Fig. 2, b), dendrite branches (Fig. 2, a, c) are grains of phase B2, probably with a three-component composition ([Ti/Ta],Ni), which are surrounded by areas with a structure of ([Ti/Ta]$_2$Ni) type. The appropriate microdiffraction pattern (Fig. 2, b) has two systems of reflections that are related to the two-phase mixture: weak quasi-ring reflections are referred to Ti_2Ni particles, the most bright reflections are referred to the matrix phase B2(TiNi). Distances between dendrite branches are from ~ 50 to ~ 100 nm and their thickness is from ~ 10 to ~ 30 nm. The bright-field image (Fig. 2, a) shows a noticeable moire pattern, which nature is related to superposition of patterns from phases Ti_2Ni and B2(TiNi).

Martensite sublayer IV with a thickness of ≤ 400 nm (Fig. 2, c) is located at a depth from $\sim 2.8\,\mu$m and composed of martensite phases B19′ and R on the basis of TiNi (Fig. 2, d) as a result of martensite transformations of the high-temperature B2(TiNi) phase under the action of residual elastic stresses caused by the LEHCEB-treatment. This conclusion is consistent with results of [25] where it has been shown that the formation of martensite in sublayers of the TiNi-substrate with SA is related to residual stresses induced by electron-beam treatments.

By the summary of structural characteristics and the distribution of tantalum as a doping element, sublayers II, III and IV can be considered as a transition zone between the [TiNi-Ta_{40}]SA and the TiNi-substrate. At a depth greater than $\sim 3.5\,\mu$m structure and composition of elements of samples with [TiNi-Ta_{40}]SA are close to the structure and composition of elements of phase B2(TiNi) for the initial TiNi-substrate.

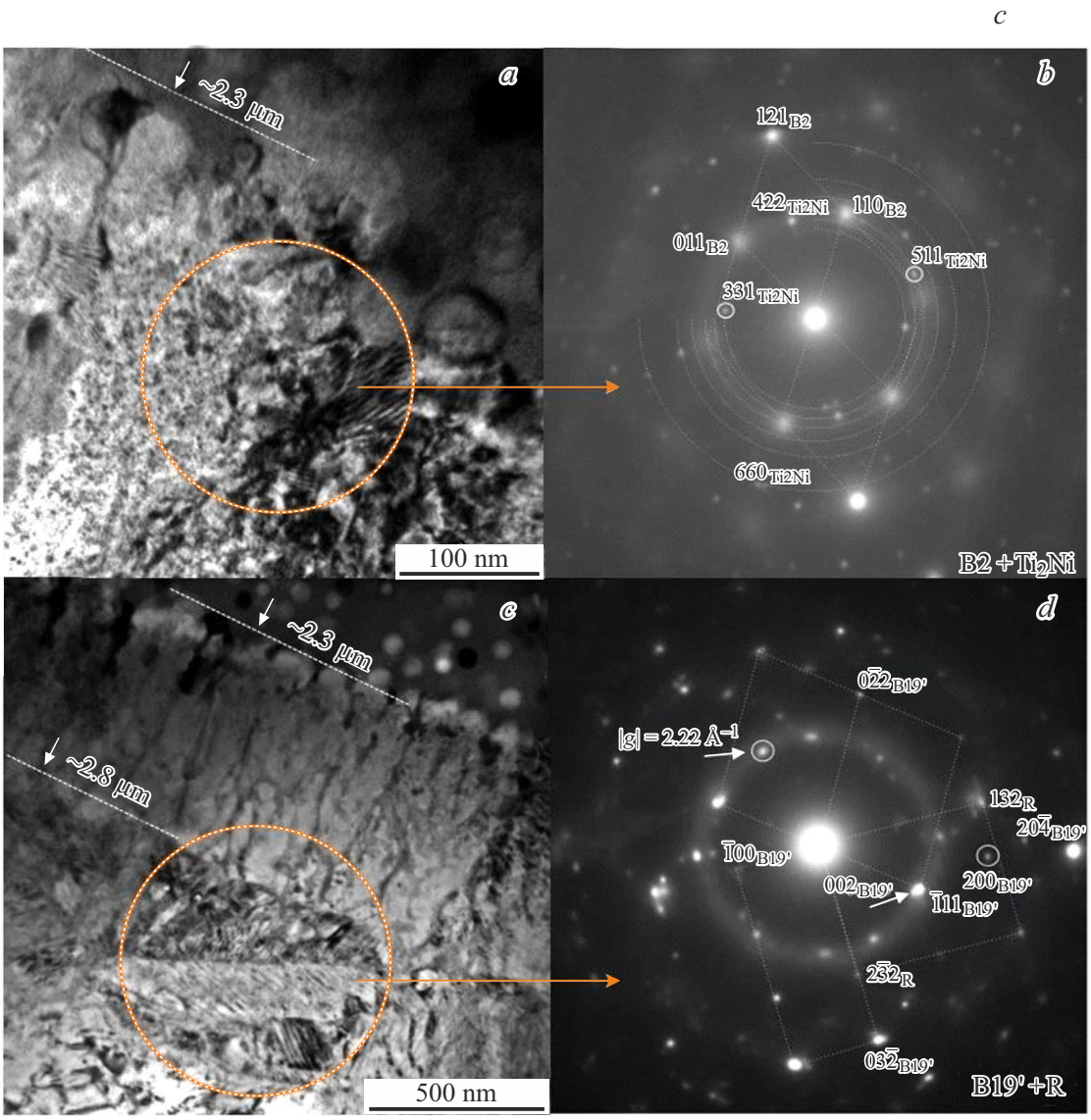

Figure 2. Bright-field images of structure of the sample with [TiNi-Ta$_{40}$]SA (a, c) and their correspondent microdiffraction patterns (b, d) from the eutectic sublayer III (a) and the martensite sublayer IV (c).

3.2. Physico-mechanical properties of the sample with [TiNi-Ta$_{40}$]SA

Let us consider, how features of structure of the [TiNi-Ta$_{40}$]SA synthesized on the surface of TiNi-substrate affect the changes in physico-mechanical properties. Fig. 4 shows an image of SA structure in the transverse cross-section and $P-h$ diagrams of „loading-unloading“ in different ranges of loads $P_{\max}$. Sublayers are separated by dashed lines and numbered with Roman numbers, phase composition is shown above each sublayer.

As can be seen from Fig. 4, the entire loading range can be divided into three sections. The first section from 5 to 60 mN (Fig. 4, b) corresponds to the change of $h_{\max}$ in the range from ~ 160 nm to $\sim 1\,\mu$m. The second section from 80 to 150 mN (Fig. 4, c) corresponds to the change of $h_{\max}$ in the range from ~ 1 to $\sim 1.8\,\mu$m. In sum, starting from the surface and down to the depth of $\sim 1.8\,\mu$m the process of deformation accumulation runs in the amorphous [TiNi-Ta$_{40}$]SA (Fig. 4, a). The third section from 170 to 300 mN (Fig. 4, d), which corresponds to a depth of $h_{\max}$ in the range from from ~ 1.8 to $\sim 2.5\,\mu$m, characterizes the accumulation of deformation in the intermediate zone (inside nanocomposite sublayer II and eutectic sublayer III (Fig. 4, a)).

It can be seen from Fig. 4, b, c that the process of deformation accumulation within the first and the second loading sections can be described by a single parabolic dependence. From this it follows that physico-mechanical properties of the [TiNi-Ta$_{40}$]SA change in a monotonous manner following a single parabolic law throughout the entire region of amorphous structure existence. With

Mechanical compatibility of the [TiNi-Ta_{40}]SA with the TiNi-substrate (where Δ is difference between values of the characteristic being compared, in absolute units and in percents)

Sample	Microhardness H_{OP}, GPa	Modulus of elasticity E_{OP}, GPa	Parameter of plasticity δ_h, %	Shape recovery ratio η, %
Initial TiNi-substrate	3.5	55	55	45
Sample with [TiNi-Ta_{40}]SA	2.8	39	66	34
Δ, abs. val.	−0.7	−16	+11	−11
Δ, %	20%	29%	20%	24%

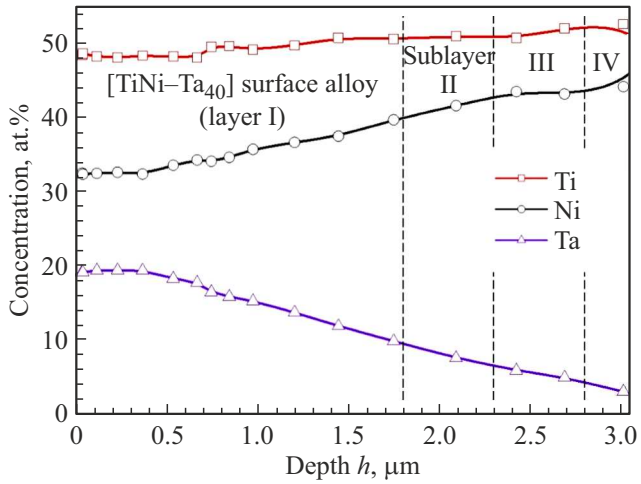

Figure 3. TEM/EDS concentration profile of element distribution in the sample with [TiNi-Ta_{40}]SA over the depth from the surface along the line marked in Fig. 1, *a*.

increase in the $P_{\max}$ load over 170 mN, when sublayers located under the [TiNi-Ta_{40}]SA become involved into the deformation under the indenter, each test cycle is described by an individual type of diagram $P-h$ (Fig. 4, *d*). Thus, within the third section of loading the recorded $P-h$ diagrams have the biggest discrepancy between the loading branch and the unloading branch and the process of deformation accumulation can not be described by a single parabolic dependence. The obtained result is a consequence of the fact that at a depth of $\sim 2.3\,\mu$m sublayers that are characterized by different structural states: nanocomposite sublayer II and eutectic sublayer III (Fig. 4, *a*) become involved into the deformation under the indenter.

Fig. 5 shows dependencies of microhardness H_{OP}, modulus of elasticity E_{OP}, plasticity parameter δ_h and shape recovery ratio η on the maximum indentation depth $h_{\max}$. As can be seen from this figure, the microhardness in the external layer I near the surface is $H_{OP} \approx 7$ GPa and monotonously decreases down to ~ 2.7 GPa at a depth of $\sim 1.8\,\mu$m (Fig. 5, curve *1*). In this case the modulus of elasticity E_{OP} also decreases monotonously from ~ 86.5 GPa at the surface down to ~ 43 GPa at the transition zone boundary (Fig. 5 curve *2*). Previously, in [5,6] it has been shown that in TiNi-samples after formation of the surface Ti-Ni-Ta-alloy with the use of $Ti_{70}Ta_{30}$ (at.%) doping film strength parameters near the surface turned to be higher ($H_{OP} \approx 8$ GPa and $E_{OP} \approx 105$ GPa) than in this [TiNi-Ta_{40}]SA. It has been shown that these higher values of H_{OP} and E_{OP} are due to the multilayer structure of this SA, which is composed of nanocrystalline sublayers following one after another.

In contrast to strength parameters (H_{OP} and E_{OP}) that change in a monotonous manner throughout the entire [TiNi-Ta_{40}]SA, the parameter of plasticity δ_h and the shape recovery ratio η change monotonously only in the near-surface layer with a thickness of ≤ 500 nm: δ_h — from ~ 58 to $\sim 65\%$ (Fig. 5, curve *3*), η — from ~ 42 to $\sim 35\%$ (Fig. 5, curve *4*). At a depth from ~ 500 nm to $\sim 1.8\,\mu$m $\delta_h(h_{\max})$ and $\eta(h_{\max})$ dependencies achieve plateau and δ_h and η parameters have their values at a level of ~ 64 and $\sim 36\%$, respectively. The behavior of plasticity parameter δ_h at a depth of ≥ 500 nm is kept at a level of $\sim 64\%$, which may be related to processes of plastic deformation of the amorphous phase: its „softening" [26] and decrease in modulus of elasticity ($E_{OP} \approx 40$ GPa).

The high degree of shape recovery ratio η equal to $\sim 42\%$ in the surface layer with a thickness of ≤ 500 nm is a direct consequence of the high modulus of elasticity on the surface ($E_{OP} \approx 86.5$ GPa). Thus, in the range of loads $P_{\max}$ from 5 to 60 mN the main mechanism of indent shape recovery on the surface of [TiNi-Ta_{40}]SA is elastic recovery. This is evidenced by $P-h$ diagrams in the range from 5 to 60 mN (Fig. 4, *b*), which unloading branches are characterized by extended sections of linear deformation return. With indentation of the [TiNi-Ta_{40}]SA down to a depth of ≥ 500 nm, the effect of lower sublayers results in that values of the η parameter decreases and achieve plateau keeping their values at a level of $\sim 36\%$.

In nanocomposite sublayer II, at a depth from ~ 1.8 to $\sim 2.3\,\mu$m strength and elastic-plastic parameters are: $H_{OP} \approx 2.7$ GPa, $E_{OP} \approx 43$ GPa, $\delta_h \approx 64\%$, $\eta \approx 36\%$. In the transition zone at the interface between nanocomposite sublayer II and eutectic sublayer III (at a depth of $\sim 2.3\,\mu$m) the loss of monotonous behavior of change in these parameters is observed. Thus, the microhardness H_{OP} and the modulus of elasticity $E_{O\Phi}$ increase from ~ 2.7 GPa and ~ 43 GPa in sublayer II to ~ 3.4 GPa and ~ 48 GPa

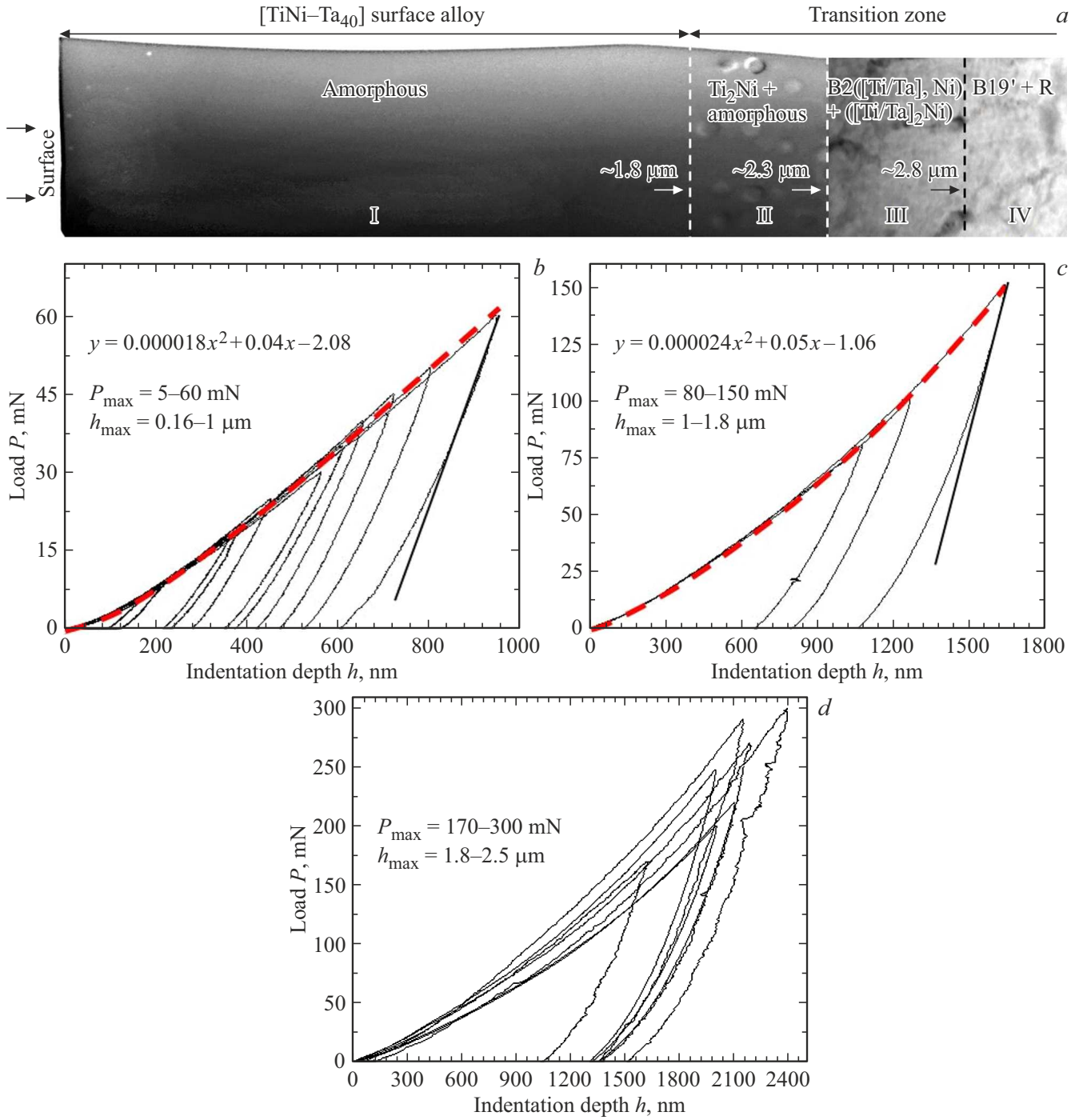

Figure 4. $P-h$ diagrams of „loading-unloading“ when the sample with [TiNi-Ta$_{40}$]SA (a) is indented in loading ranges: 5–60 (b), 80–150 (c) and 170–300 mN (d).

in sublayer III. The plasticity parameter δ_h decreases from $\sim 64\%$ in sublayer II to $\sim 61\%$ in sublayer III. The degree of indent recovery η increases from ~ 36 to $\sim 39\%$. Taking into account the information on the structure (Fig. 1, 2), the deformation behavior ($P-h$ diagrams (Fig. 4, d)) and properties (Fig. 5), it can be stated that the loss of monotonous character of change in parameters at the interface between nanocomposite sublayer II and eutectic sublayer III is due to the difference of structure and phase composition between these sublayers. In eutectic sublayer III, at a depth from $\sim 2.3\,\mu$m strength and elastic-plastic parameters are: $H_{OP} \approx 2.8$ GPa, $E_{OP} \approx 39$ GPa, $\delta_h \approx 66\%$, $\eta \approx 34\%$.

To evaluate the mechanical compatibility between the SA and the TiNi-substrate, a comparison is carried out between the strength and elastic-plastic parameters for the initial

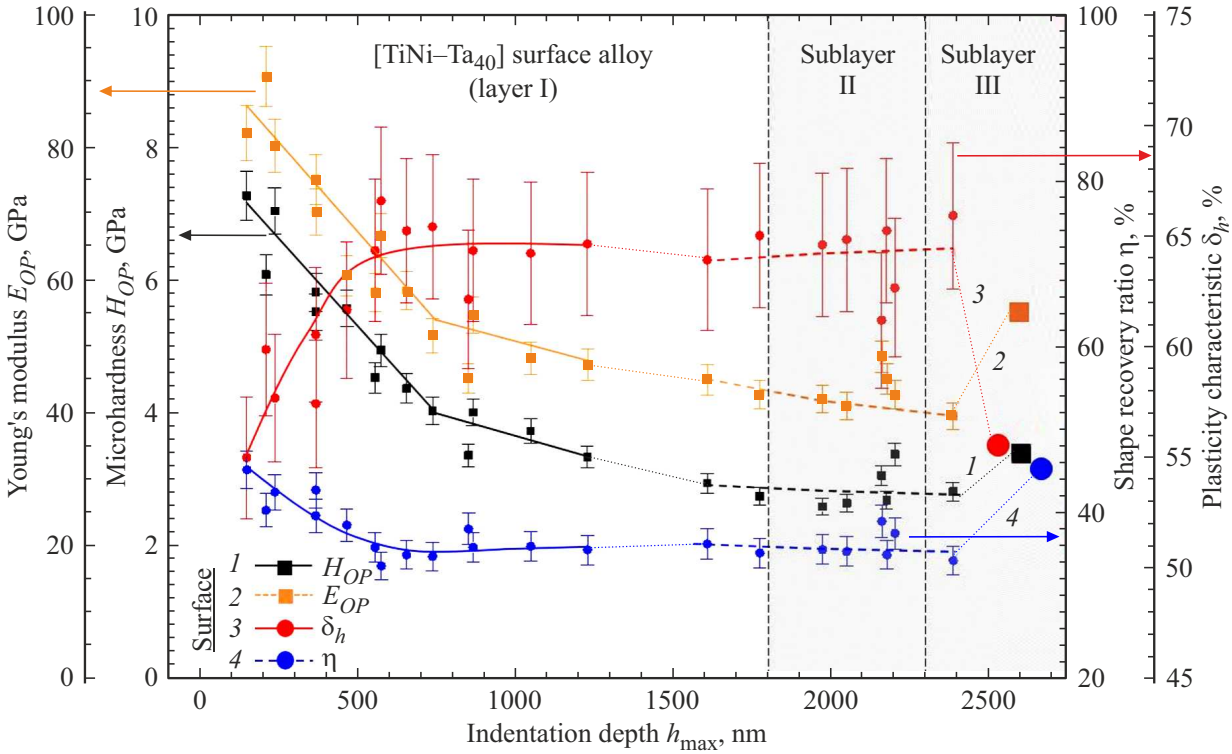

Figure 5. Dependence of microhardnessH_{OP} (*1*), elastic modulus E_{OP} (*2*), plasticity parameter δ_h (*3*) and indent recovery degree η (*4*) on the maximum indentation depth h_{max} for the sample with [TiNi-Ta$_{40}$]SA (large symbols show properties for the initial TiNi-substrate at a depth more than $\sim 2\,\mu$m).

TiNi-substrate and values of these parameters for the sample with [TiNi-Ta$_{40}$]SA obtained at a depth of $\sim 2.5\,\mu$m (table).

As can be seen from the table, the differences between values of strength and elastic-plastic characteristics of the [TiNi-Ta$_{40}$]SA and the initial TiNi-substrate are not more than $\sim 20-30\%$. At the same time, the lower values of H_{OP} and E_{OP} in the sample with [TiNi-Ta$_{40}$]SA are related to the formation of martensite phases B19′ and R(TiNi) in sublayer IV (Fig. 2, *c*, *d*), which, as known [18], are characterized by lower values of H_{OP} and E_{OP}, as compared with the phase B2(TiNi). The presence of martensite in sublayer IV probably has resulted in keeping high plasticity at a depth of $\sim 2.5\,\mu$m in the sample with [TiNi-Ta$_{40}$]SA ($\delta_h \approx 66\%$, Fig. 5, curve *3*).

4. Conclusion

Thus, in this study the method of additive thin-film electron beam synthesis has been used to form amorphous [TiNi-Ta$_{40}$]SA on the surface of the TiNi-substrate using Ti$_{60}$Ta$_{40}$ (at.%) doping film. Based on the data obtained by transmission electron microscopy and instrumented indentation, the following conclusions are formulated regarding the relation of the structure of surface alloy and the transition zone to the physico-mechanical properties.

1. External amorphous layer I, which is the [TiNi-Ta$_{40}$]SA, has ~ 2 and ~ 1.5 times higher values of the microhardness H_{OP} and the modulus of elasticity E_{OP} than those of the initial TiNi-substrate and close to it values of elastic-plastic parameters: the plasticity δ_h and the degree of shape recovery ratio η.

2. Changes in physico-mechanical properties of the [TiNi-Ta$_{40}$]SA and the transition zone are due to the quantity and thickness of sublayers, as well as the effect of structural states of phases in sublayers (amorphous, nanocomposite and nanocrystalline).

3. The mechanical compatibility of the synthesized [TiNi-Ta$_{40}$]SA and the TiNi-substrate expressed as a difference between strength and elastic-plastic characteristics is not more $\sim 20-30\%$. As a result of the work performed, it is important to note that the high mechanical compatibility between the synthesized layers of SA and the TiNi-substrate is of practical importance for miniature products for healthcare and non-healthcare purposes manufactured from TiNi alloys.

Funding

This study was carried out by the Government research assignment for Institute of Strength Physics and Materials Science, project FWRW-2021-0003.

Conflict of interest

The authors declare that they have no conflict of interest.

References

[1] J.J. Mohd, M. Leary, A. Subic, M.A. Gibson. Mater. Des. **56**, 1078 (2014). DOI: 10.1016/j.matdes.2013.11.084

[2] V. Iasnii, P. Yasniy. Acta Mechanica Automatica **13**, 95 (2019). DOI: 10.2478/ama-2019-0013

[3] Y. Say, B. Aksakal. J. Mater. Res. Technol. **9**, 1742 (2020). DOI: 10.1016/j.jmrt.2019.12.005

[4] C.L. Chu, R.M. Wang, T. Hu, L.H. Yin, Y.P. Pu, P.H. Lin, S.L. Wu, C.Y. Chung, K.W.K. Yeung, P.K. Chu. Mater. Sci. Eng. C **28**, 1430 (2008). DOI: 10.1016/j.msec.2008.03.009

[5] L.L. Meisner, A.B. Markov, V.P. Rotshtein, G.E. Ozur, S.N. Meisner, E.V. Yakovlev, V.O. Semin, Yu.P. Mironov, T.M. Poletika, S.L. Girsova, D.A. Shepel. J. Alloys Compd. **730**, 376 (2018). DOI: 10.1016/j.jallcom.2017.09.238

[6] S.N. Meisner, E.V. Yakovlev, V.O. Semin, L.L. Meisner, V.P. Rotshtein, A.A. Neiman, F. D'yachenko. Appl. Surf. Sci. **437**, 217 (2018). DOI: 10.1016/j.apsusc.2017.12.107

[7] L.L. Meisner, V.P. Rotshtein, V.O. Semin, A.B. Markov, E.V. Yakovlev, S.N. Meisner, D.A. Shepel, A.A. Neiman, E.Yu. Gudimova, F.A. D'yachenko, R.R. Mukhamedova. Mater. Charact. **166**, 110455 (2020). DOI: 10.1016/j.matchar.2020.110455

[8] L.L. Meisner, V.P. Rotshtein, V.O. Semin, S.N. Meisner, A.B. Markov, E.V. Yakovlev, F.A. D'yachenko, A.A. Neiman, E.Yu. Gudimova. Surf. Coat. Technol. **404**, 126455 (2020). DOI: 10.1016/j.surfcoat.2020.126455

[9] V.O. Semin, M.G. Ostapenko, L.L. Meisner, F.A. D'yachenko, A.A. Neiman. Appl. Phys. A **128**, *1*, 664 (2022). DOI: 10.1007/s00339-022-05815-3

[10] A. Bahrami, J.P. Alvarez, O. Depablos-Rivera, R. Mirabal-Rojas, A. Ruiz-Ramirez, S. Muhl, S.E. Rodil. Adv. Eng. Mater. **20**, *1*, 1700687 (2017). DOI: 10.1002/adem.201700687

[11] T. Burgess, M. Ferry. Mater. Today **12**, 24 (2009). DOI: 10.1016/S1369-7021(09)70039-2

[12] W. Guo, E. Jagle, J. Yao, V. Maier, S. Korte-Kerzel, J.M. Schneider, D. Raabe. Acta Mater. **80**, 94 (2014). DOI: 10.1016/j.actamat.2014.07.027

[13] J. Pfetzing, M.F.-X. Wagner, T. Simon, A. Schaefer, Ch. Somsen, G. Eggeler. ESOMAT, **2009**, **1**, 06027 (2009). DOI: 10.1051/esomat/200906027

[14] W. Ni, Y.-T. Cheng. Appl. Phys. Lett. **82**, **1**, 2811, (2003). DOI: 10.1063/1.1569984

[15] M. Mohri, M. Nili-Ahmadabadi, J. Ivanisenko, R. Schwaiger, H. Hahn, V.S.K. Chakravadhanula. Thin Solid Films **583**, 245 (2015). DOI: 10.1016/j.tsf.2015.03.057

[16] G. Pan, Z. Cao, J. Shi, M. Wei, L. Xu, X. Meng. Sens. Actuators **217**, 75 (2014). DOI: 10.1016/j.sna.2014.06.019

[17] W.C. Oliver, G.M. Pharr. J. Mater. Res. **19**, 3 (2004). DOI: 10.1557/jmr.2004.19.1.3

[18] Q. Kan, W. Yan, G. Kang, Q. Sun. J. Mech. Phys. Solids **61**, 2015 (2013). DOI: 10.1016/j.jmps.2013.05.007

[19] Yu.V. Milman. J. Phys. D **41**, *1*, 074013 (2008). DOI: 10.1088/0022-3727/41/7/074013

[20] Y. Ye, Z. Liu, W. Liu, D. Zhang, Y. Wang, H. Zhao, X. Li. RSC Adv. **8**, 5596 (2018). DOI: 10.1039/C7RA12409K

[21] Patent 2017137653/15(065731) The Russian Federation, MPK A61L 27/06, B82B 1/00, C22C 45/10, A61L 31/18, C22C 45/04, C23C 28/00. Method for synthesis of a radiopaque surface Ti-Ta-Ni alloy with an amorphous or amorphous-nanocrystalline structure on TiNi alloy substrate, L.L. Meisner, A.B. Markov, G.E. Ozur, V.P. Rotshtein, S.N. Meisner, E.V. Yakovlev, E.Yu. Gudimova, V.O. Semin, Patent holder ISPMS SB RAS, IHCE SB RAS, Publ. 11.04.18 (in Russian).

[22] A.R. Dujovne, J.D. Bobyn, J.J. Krygier, J.E. Miller, C.E. Brooks. J. Arthroplasty **8**, 7 (1993). DOI: 10.1016/s0883-5403(06)80102-6

[23] N. Soro, H. Attar, E. Brodie, M. Veidt, A. Molotnikov, M.S. Dargusch. J. Mech. Behav. Biomed. Mater. **97**, 149 (2019). DOI: 10.1016/j.jmbbm.2019.05.019

[24] G.E. Ozur, D.I. Proskurovsky. Plasma Phys. Rep. **44**, 18 (2018). DOI: 10.1134/S1063780X18010130.

[25] M.G. Ostapenko, V.O. Semin, F.A. D'yachenko, A.A. Neiman, L.L. Meisner. Acta Mater. **231**, 117893(1) (2022). DOI: 10.1016/j.actamat.2022.117893

[26] T.C. Hufnagel, C.A. Schuh, M.L. Falk. Acta Mater. **109**, 375 (2016). DOI: 10.1016/j.actamat.2016.01.049

Translated by Y.Alekseev